16th Australasian Fluid Mechanics Conference
Crown Plaza, Gold Coast, Australia
2-7 December 2007

Eigen-analysis of Inviscid Fluid Structure Interaction (FSI) Systems with Complex Boundary Conditions

A. D. Lucey and M. W. Pitman

Fluid Dynamics Research Group
Curtin University of Technology, Western Australia, 6845 AUSTRALIA

Abstract

A method for extracting the eigenvalues and eigenmodes from complex coupled fluid-structure interaction (FSI) systems is presented. The FSI system under consideration in this case is a one-sided, inviscid flow over a finite-length compliant surface with complex boundary conditions, although the method could be applied to any FSI system. The flow is solved for the inviscid case using a boundary-element method solution of Laplace's equation, while the finite compliant surface is solved through a finite-difference solution of the one-dimensional beam equation. The crux of the method lies in reducing the coupled fluid and structural equations down to a set of coupled linear differential equations. Standard Krylov subspace projection methods may then be used to determine the eigenvalues of the large system of linear equations. This method is applied to the analysis of hydroelastic FSI systems with complex boundary conditions that would be difficult or otherwise impossible to analyse using standard Galerkin methods. Specifically, the complex cases of inhomogeneous and discontinuous compliant wall properties and arbitrary hinge-joint conditions along the compliant surface are considered.

Introduction

Numerical methods are used to investigate the stability of a finite-length compliant wall interacting with an incompressible, high-Reynolds number, boundary layer flow over one side. In the limit of infinite Reynolds number, the flow may be modelled using an inviscid approximation. A schematic of the fluid-structure system is presented in Figure 1. The compliant wall is composed of a simple elastic plate that may have an added spring foundation and structural damping.
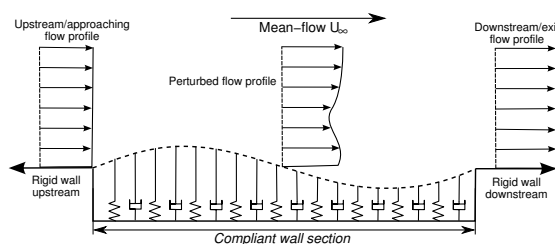

Figure 1: Schematic of the flow-structure system studied; the spring and dashpot foundations are absent for an unsupported elastic plate.

The problem of a one-sided *infinitely-long* compliant wall interacting with an inviscid flow is well documented through theoretical studies by Carpenter and Garrad [1].

This paper presents a technique whereby the fluid-structure system for a finite wall is represented as a single governing set of linear equations. Some simple results will be presented that may be validated against existing results obtained through theoretical or Galerkin methods. Finally, the new method will be

used to perform an illustrative investigation into the complex wall behaviour with more complex inhomogeneous conditions and multiple hinged boundary conditions imposed.

System equations

The linear motion of the compliant wall is governed by the two-dimensional beam equation. Extra terms are added to account for the addition of homogeneous backing springs ($K\eta$) and uniform dashpot-type damping ($d\partial\eta/\partial t$) to model the effects of energy dissipation in the wall structure.

$$\rho_m h\frac{\partial^2 \eta}{\partial t^2} + d\frac{\partial \eta}{\partial t} + B\frac{\partial^4 \eta}{\partial x^4} + K\eta = -\Delta p(x,0,t) \ , \qquad (1)$$

where $\eta(x,t)$, ρ_m, h and B are, respectively, the plate's deflection, density, thickness and flexural rigidity, while $p(x,y,t)$ is the unsteady fluid pressure. In the present problem we apply hinged-edge conditions at the leading and trailing edges of the plate although in the method that follows there is no necessary restriction on such boundary conditions.

The fluid is modelled using the assumptions of incompressible and irrotational flow. This is an appropriate approximation for the high Reynolds number flow outside the boundary layer, however rotationality and viscous effects of the boundary layer are ignored. This therefore implies the approximation that the boundary layer is thin with respect to the wall disturbance wavelength and amplitude. A velocity perturbation potential $\phi(x,y,t)$ which satisfies Laplace's equation is introduced and the solution of which is then used in the linearised unsteady Bernoulli equation,

$$\Delta p = -\rho\frac{\partial \phi}{\partial t} - \rho U_\infty \frac{\partial \phi}{\partial x} \ , \qquad (2)$$

where ρ and U_∞ are, respectively, the fluid density and flow speed. The plate and fluid motions are coupled through the boundary condition of zero normal velocity at the wall and a balance of unsteady pressure forces.

Eigenvalue Determination

A Single Governing Equation for the System

Where Lucey and Carpenter [2] used an explicit time-marching scheme for the solution of the wall position, the objective here is to avoid temporal discretisation by direct solution of a single set of ordinary differential equations. The compliant wall position, $\eta(x,t)$, will be the single resulting variable.

Due to the linearity of Laplace's equation, the boundary element solution for the fluid equation may be expressed as the sum of a mean flow plus a distribution of singularities along the deforming compliant wall. In this case, zero order linear source(-sink) elements are chosen for the singularities, with the strength of each element denoted $\sigma(x)$. With the discretisation of the compliant surface into N elements, each with constant strength σ_i, the vector of element strengths may be determined through a

balance of the normal velocity components at the wall

$$\{\sigma\} = 2U_\infty[D_1]\{\eta\} + 2\{\dot{\eta}\} \quad , \qquad (3)$$

where $\{\eta\}$ is the vector of interfacial displacements at the N evaluation points, the overdot denotes time-differentiation, and $[D_1]$ is the first-order spatial differentiation finite-difference matrix operator.

The singularity strengths (σ) determined through Eqn. 3 may be used to evaluate the tangential velocity and perturbation potential at each element along the compliant surface. Substitution of these expressions and Eqn. 3 into the unsteady Bernoulli equation, Eqn. 2, yields an expression for the forcing pressure at the wall in terms of interfacial displacement alone to give

$$\begin{aligned} -\{\Delta p\} = & 2\rho U_\infty^2[T][D_1]\{\eta\} + 2\rho U_\infty[T]\{\dot{\eta}\} \\ & + 2\rho U_\infty[T][\Phi]\{\dot{\eta}\} + 2\rho[\Phi]\{\ddot{\eta}\} \quad , \end{aligned} \qquad (4)$$

where $[T]$ is the matrix of tangential-velocity influence coefficients. The form of Eqn. 4 shows the pressure to comprise the hydrodynamic stiffness (curvature effects), followed by two terms that yield the hydrodynamic damping (Coriolis' effects) and the final term that represents the hydrodynamic inertia (added-mass effects). The solution method for the flow field is described in more detail in Lucey *et al.* [3] wherein expressions for the various influence coefficients are listed.

The wall equation, Eqn. 1, may be couched in finite-difference form using a set of N lumped-mass points that corresponds to the boundary-element panel control points. Substituting the pressure-perturbation vector of Eqn. 4 into this finite difference expression gives

$$\{\ddot{\eta}\} = [E]\{\dot{\eta}\} + [F]\{\eta\} \quad , \qquad (5)$$

where

$$\begin{aligned} [E] = & (\rho_m h[I] - 2\rho[\Phi])^{-1} \times \\ & (2\rho U_\infty[T] + 2\rho U_\infty[T][\Phi] - d[I]) \quad , \\ [F] = & (\rho_m h[I] + 2\rho[\Phi])^{-1} \times \\ & \left(2\rho U_\infty^2[T][D_1] - B[D_4][\Phi] - K[I] \right) \quad . \end{aligned}$$

where $[I]$ is the identity matrix and $[D_4]$ is the fourth-order spatial differentiation (penta-diagonal) matrix operator.

State-Space Solution

We now solve Eqn. 5 using a standard state-space method. The second order $N \times N$ system is transformed to the following first-order $2N \times 2N$ system

$$\{\dot{w}\} = [H]\{w\} \quad , \qquad (6)$$

where

$$[H]\{w\} = \begin{bmatrix} 0 & I \\ -F & E \end{bmatrix} \left\{ \begin{array}{c} \{\eta\} \\ \{\dot{\eta}\} \end{array} \right\} \quad , \qquad (7)$$

for the new variable w. Assuming that all parts of the system move with the complex frequency, $s = s_R + is_I$, we can write

$$w = W \exp(st) \quad , \qquad (8)$$

and substituting this into Eqn. 6, yields

$$(s[I] - [H])\{W\} = 0 \quad , \qquad (9)$$

and the solution of $\det(s[I] - [H]) = 0$ then generates the eigenvalues. These have been evaluated using the ARPACK solver

through the EIGS command in the MATLAB software. Having found the eigenvalues, these can then, in turn, be substituted back into Eqn. 9 to extract the complex eigenmode, $\{W\}^T$ for the N interfacial points.

Results

In the results presented in this section, we use the non-dimensional scheme of [3]. This scheme is appropriate for the finite system studied here. The non-dimensional control parameter (stiffness ratio) and time are given by

$$\Lambda^F = \frac{\rho U_\infty^2 L^3}{B} \quad , \quad t' = \left\{ \frac{\sqrt{B/\rho_m h}}{L} \right\} \left(\frac{1}{h} \right) t \quad . \qquad (10a, b)$$

Additionally, for cases where structural damping is introduced, the non-dimensional damping coefficient is,

$$d' = \left(\frac{L^2}{2\sqrt{\rho_m(B\pi^4 + KL^4)}} \right) d \quad , \qquad (11)$$

with $K = 0$ for a simple flexible plate.

Subplots (a) and (b) within each Figure show the variation of eigenvalues with flow-to-wall stiffness ratio (applied flow speed for a plate of given properties) for the imaginary (oscillatory) part (a) and the real (positive = growth, negative = decay) part (b) respectively.

Subplots (c), (d) and (e) show snapshots of the wall motion for various specific eigenvalues that are marked on subplots (a) and (b). For all snapshots of the wall motion in (c)-(e), the thick line indicates the final wall position in the time-sequence of plots.

First, some results will be presented for a simple elastic plate. This is the first time that 'exact' eigenvalues have been extracted for the fluid-structure problem. The case of a simple elastic plate also provides a base for validation of the method with previous work. Results will then be presented for simple plates with more complex boundary conditions, including inhomogeneous wall properties and multiple hinged boundary conditions.

Simple elastic plate

Figure 2 shows the variation of eigenvalues and with non-dimensional stiffness ratio. The stiffness ratio Λ^F could be interpreted as a measure of the flow speed for some given plate properties. Figures 2a and 2b are the variation of the non-dimensional oscillatory s'_I and growth/decay s'_R parts of the eigenvalues respectively. The solution can be broken into four regions, being: a neutrally stable pre-divergence region, a divergence loop, a small neutrally stable divergence recovery zone, and finally a region of modal coalescence flutter. Figures 2c, 2d and 2e show snapshots of the wall motion for the most unstable modes in the pre-divergence, divergence and divergence-recovery zones respectively. These wall-position snapshots are the eigenmodes that correspond to the eigenvalues at specific points on Figures 2a and 2b.

Inhomogeneous flexible plates

Figure 3 shows the variation of eigenvalues and eigenmode snapshots for a wall with identical properties as the simple elastic plate shown in Figure 2, except that the flexural rigidity parameter of the wall (B) is varied linearly along the length of the wall. In this case, the mean value of the flexural rigidity (B_{AV}) is identical to that of Figure 2 and the non-dimensional stiffness ratio Λ^F is based on this value. The gradient is set so that B varies from $1.95B_{AV}$ at the upstream edge down to $0.05B_{AV}$ at the trailing edge.
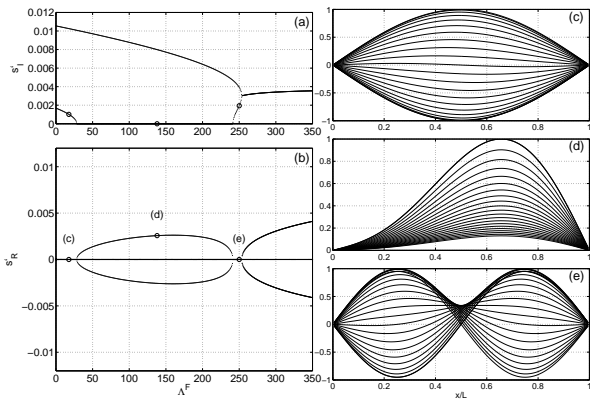
Figure 2: Elastic-plate. Eigenvalues and snapshots of wall motion at various flow speeds, Mode-1 amplifying, for $t' : 0 \rightarrow 793$ over 20 time steps each of duration $\Delta t' = 39.6$ at: (c) $\Lambda^F = 17.6$, (d) $\Lambda^F = 138$, and (e) $\Lambda^F = 250$.

Figures 3c, 3d and 3e show snapshots of the most unstable eigenmodes at various stages throughout the divergence loop. Qualitatively, the form of both the eigenvalue and eigenmode plots of Figure 3 are similar to Figure 2. However, the addition of a linear variation of the flexural rigidity such that the upstream end is more rigid than the downstream end tends to push the divergence loop down and to the right. This indicates that stiffening the upstream half of an elastic plate tends to stabilise the system in a similar manner to the addition of structural damping. Interestingly, numerical experiments performed with a stiffened a downstream end tended to destabilise the system by pushing the divergence loop up and to the left.
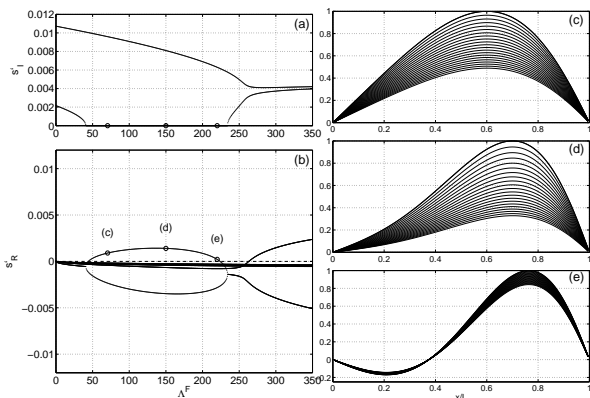

Figure 3: Elastic plate with material inhomogeneity. Eigenvalues and snapshots of wall motion in the divergence range of flow speeds, Mode-1 amplifying, for $t' : 0 \rightarrow 793$ over 20 time steps each of duration $\Delta t' = 39.6$ at: (c) $\Lambda^F = 70.5$, (d) $\Lambda^F = 150$, and (e) $\Lambda^F = 220$.

Multiple hinged boundary conditions

Figure 4 shows results for the same elastic plate as used for Figure 2, except that an extra hinge constraint has been added at a distance of $0.3L$ from the upstream edge. Note the increased range of values of Λ^F over which the eigenvalues are plotted.

For the fundamental (most unstable) mode, there exists a pre-divergence range where wall motion is slightly attenuated, however the third mode is unstable in this pre-divergence range. There is then a divergence loop that leads into modal
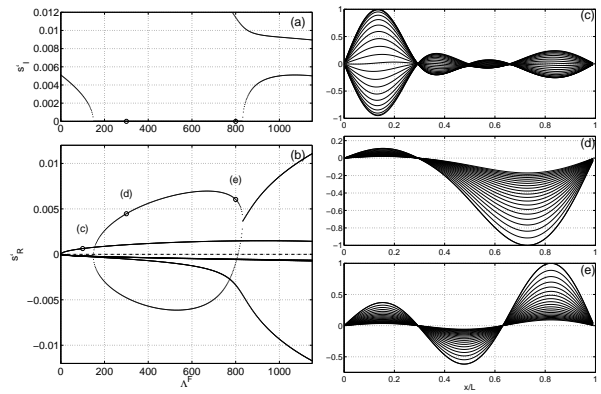

Figure 4: Elastic plate with a boundary constraint at 30% chord. Eigenvalues and snapshots of wall motion, for $t' : 0 \rightarrow 396$ over 20 time steps each of duration $\Delta t' = 19.8$ for: Mode-3 amplifying for (c) $A^F = 100$, and Mode-1 amplifying for (d) $A^F = 300$, and (e) $A^F = 800$.

coalescence-flutter type instability with no post-divergence recovery zone. The primary differences with the simple elastic plate of Figure 2 are: a) the attenuation of most modes in the pre-divergence range; b) the increased stability of the system as a whole with the divergence onset occurring at much larger values of Λ^F; c) the lack of a post-divergence recovery zone and; d) a specific mode becomes unstable at low values of Λ^F, in the limit of $\Lambda^F \rightarrow 0$.

The increased stability of the system could be anticipated due to the fact that a hinge joint shortens the effective length of the elastic plate. Basing Λ^F on the length of the longest part of the divided wall places the divergence loop into a similar range of values as Figure 2. However, it is interesting to note the introduction of a new instability that occurs in the limit of zero flow speed. Figure 4c reveals that this principally comprises the third in-vacuo mode which seems to be destabilised by the addition of the hinge joint.

Figure 5 is for the same configuration as Figure 4, except that the hinge joint has been placed at $0.5L$. The shape of the eigenvalue loci in Figure 5 differs from Figures 4 and 2 in that two divergence loops may be observed. Figures 5c and 5d show the corresponding eigenmode snapshots for the inner and outer divergence loops respectively at $\Lambda^F = 1000$. Two divergence loops appear because the addition of a hinge joint at 50% introduces more possible configurations for instability to occur. Divergence-type instability may occur on either half of the divided panel with each half destabilising in-phase or out-of-phase (as seen in Figures 5c and 5d respectively). There also exists a small amount of higher-mode instability in the limit of $\Lambda^F \rightarrow 0$, although this instability is not as severe as in Figure 4.

Figure 6 shows results for the same wall parameters and hinge conditions as in Figure 4, except that a small amount of structural damping is added to the flexible wall. This small amount of structural damping has no noticeable effect on the shape or position of the divergence loop and its mode shapes. However, the addition of the structural damping does shift the eigenvalue loci of the higher modes downwards in Figure 6b. This eliminates the higher-mode instability in the pre-divergence range.

Figure 7 shows results for the same wall parameters and hinge conditions as in Figure 4, except that the hydrodynamic damping term ($[E]$ in Eqn. 5) has been set to zero. This does not
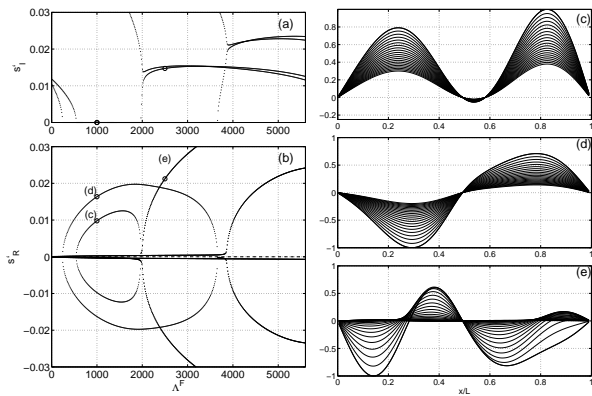
Figure 5: Elastic plate with a boundary constraint at 50% chord. Eigenvalues and snapshots of wall motion, for $t' : 0 \rightarrow 99$ over 20 time steps each of duration $\Delta t' = 4.95$ for: (c) Mode-1 amplifying for $A^F = 1000$, (d) Mode-2 amplifying for $A^F = 1000$, and (e) Mode-3 amplifying for $A^F = 2500$.
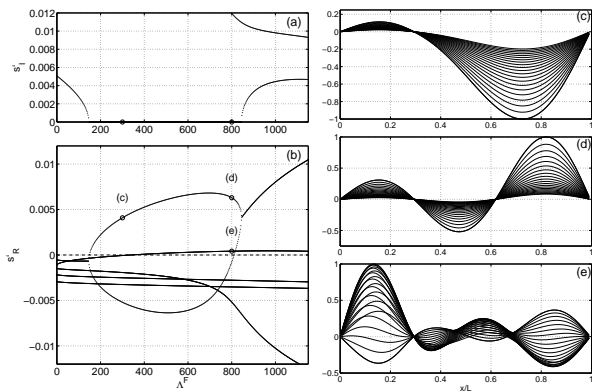

Figure 6: Elastic plate the same parameters and addition hinge condition as Figure 4, except that a small amount of structural damping $d' = 0.082$ is added. Eigenvalues and snapshots of wall motion, for $t' : 0 \rightarrow 396$ over 20 time steps each of duration $\Delta t' = 19.8$ for: Mode-1 amplifying for (c) $A^F = 300$, (d) $A^F = 800$, and Mode-2 amplifying for (e) $A^F = 800$.

correspond to any physical possibility, and therefore could not occur in reality. In this case, divergence-onset occurs at the same point as in Figure 4, however no divergence loop is created from this point, nor does divergence recovery occur. Likewise, the higher-mode pre-divergence instability is eliminated and replaced with neutral stability of all modes in the pre-divergence range. Figures 7d and 7e show that, unlike Figure 4, the divergence mode shape is not forced in the downstream direction. This is principally noticed through comparison of Figure 4e, where the mode is forced downstream to the extent that it appears almost as the second *in-vacuo* mode, and Figure 7e where the first mode remains relatively unchanged. Thus the action of the hydrodynamic damping term tends to force the mode shape downstream for an unstable growing mode. At sufficiently high wave travel (and growth) rates, this downstream forcing of the mode shape transforms the fundamental mode into the second mode (as seen in Figures 4d and 4e). While the effect of this forcing due to the hydrodynamic damping term is most evident throughout the divergence range of flow speeds, it still occurs at lower, pre-divergence flow speeds, causing the mode shape to waver upstream and downstream as it oscillates in its neutrally stable state. The elimination of higher-mode pre-divergence instability with the removal of the structural damping term could
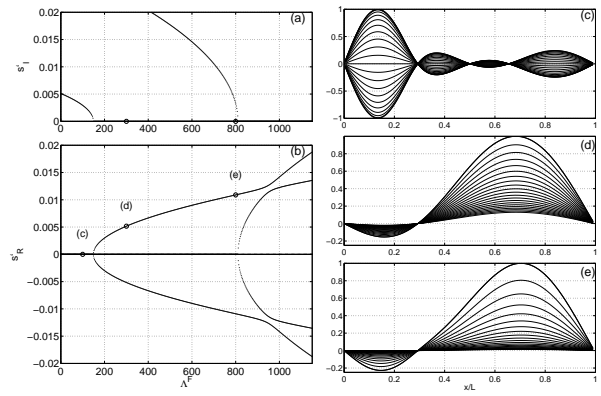

Figure 7: Elastic plate the same parameters and addition hinge condition as Figure 4, except that the hydrodynamic damping term is set to 0. Eigenvalues and snapshots of wall motion, for $t' : 0 \rightarrow 396$ over 20 time steps each of duration $\Delta t' = 19.8$ for: Mode-1 amplifying for (c) $A^F = 100$, (d) $A^F = 300$, and (e) $A^F = 800$.

indicate that this instability is brought about by different phase relations (between wall motion and fluid damping) on either side of the added hinge. More numerical experiments are needed to confirm this hypothesis.

Conclusions

This paper presents the use of linear discretisation and Krylov methods for eigenvalue extraction from large matrices to give accurate determination of linearised fluid-structure interaction problems. These methods were then applied to the determination of eigenvalue loci and corresponding eigenmodes for a simple elastic plate with complex boundary conditions.

Increasing the rigidity of the flexible plate at the upstream end was found to stabilise the structural system, while stiffening of the downstream end tended to destabilise the system. The addition of a hinge joint was found to stabilise the system by decreasing the effective length of the flexible plate, however it also made the plate prone to a higher mode instability that persists to very low values of Λ^F. This higher-mode pre-divergence instability could be a result of forcing communication between the parts of the plate either side of the hinge joint.

Acknowledgements

References

[1] Carpenter, P.W. and Garrad, A.D., The hydrodynamic stability of flows over Kramer-type compliant coatings. Part 1. Tollmien-Schlichting instabilities. *Journal of Fluid Mechanics*, **155**, 1985, 465–510.

[2] Lucey, A.D. and Carpenter, P.W., A numerical simulation of the interaction of a compliant wall and inviscid flow. *Journal of Fluid Mechanics*, **234**, 1992, 121–146.

[3] Lucey, A. D., Carpenter, P.W., Cafolla, G. J. and Yang, M., The Nonlinear Hydroelastic Behaviour of Flexible Walls. *Journal of Fluids and Structures*, **11**, 1997, 717–744.